Applied Ocean Research 78 (2018) 180–191

Contents lists available at ScienceDirect

Applied Ocean Research

journal homepage: www.elsevier.com/locate/apor

Hydrodynamic modeling of a novel dual-chamber OWC wave energy converter

Dezhi Ning[a,b], Yu Zhou[a,b], Chongwei Zhang[a,b,*]

[a] State Key Laboratory of Coastal and Offshore Engineering, Dalian University of Technology, Dalian 116024, China
[b] Offshore Renewable Energy Research Center, Dalian University of Technology, Dalian 116024, China

ARTICLE INFO

Keywords:
Oscillating water column
Wave energy converter
Eigenfunction expansion
Potential flow theory
Dual-chamber

ABSTRACT

A novel cylindrical oscillating water column (OWC) wave energy converter (WEC) with double chambers is proposed to harvest the wave energy effectively in deep water. An analytical model is developed to investigate its hydrodynamic characteristics based on the linear potential flow theory and eigenfunction expansion technique. The computational domain is divided into six sub-domains. The unknowns are solved by matching the continuous conditions of the fluid velocity and velocity potential between neighboring sub-domains. A pneumatic model is adopted to describe the relationship between the air pressure in the chamber and turbine characteristics. Effects of the chamber volume and parameters of the turbine on the energy conversion efficiency are investigated. It is found that the chamber volume affects the OWC hydrodynamics seriously in the case of large turbine rotating speed. Three typical free-surface oscillation modes in the chamber are found, two of which contribute much to the energy conversion. The comparison between results of the single- and dual-chamber OWC-WECs shows that the effective frequency bandwidth of the dual-chamber OWC-WEC is broader than that of the single-chamber OWC-WEC.

1. Introduction

The ocean waves contain tremendous energy potential. Up to now, there have been a variety of wave energy converters (WECs) invented to capture the energy from waves, some of which have already undergone prototype experiments aiming at commercialization [1]. However, the WEC techniques have not converged into one technical stream as that in the wind energy field at the present stage of development. Among various WECs [2–5], the oscillating water column (OWC) WEC has been considered as one of the most promising options [6]. The OWC-WEC is characterized by the air chamber with a subsurface opening at the bottom and a bi-directional air turbine on the top. In the operation, waves enter the chamber and cause the captured water column to move up and down like a piston, forcing a bi-directional air flow through the turbine to generate electricity.

After the first OWC-WEC was invented in Japan [7], different shoreline bottom-fixed OWC-WEC concepts have been proposed and tested in prototype, such as the Sakata (60KW) in Japan [8], the Pico plant (400KW) in Portugal [9], the Islay plant (500KW) in UK [10], and the shoreline OWC (100KW) in China [11]. Theoretical and experimental studies of OWC-WECs have been carried out in the literature. For example, the land-based OWC-WECs were analyzed by Evans and Porter [12], Koo and Kim [13], Sentürk and Özdamar [14], Luo et al. [15], Ning et al. [16,17], Sentürk et al. [18], Mora et al. [19] and so on. However, shoreline fixed OWC-WECs are limited to the deployment in finite water depth and therefore exposed to a lower level of energy flow density.

Compared with the finite water depth, the deep water means a high level of energy flow density which has attracted the attention of international scholars. Zhu and Mitchell [20] presented an analytical solution of ocean wave diffractions around a hollow cylindrical shell structure. Gomes et al [21] investigated the optimization of a spar-type floating OWC-WEC, and found that the diameter of the floater, the submerged length and air chamber height influence the annual average power significantly. Konispoliatis [22] derived an analytical solution based on the linear potential-flow theory to study the hydrodynamics of an array of OWC-WECs. Three-unit arrays are discussed which can be used as multi-purpose floating structure suitable for offshore wind and wave energy sources exploitation. Gomes et al. [23] developed a double-heaving-body numerical model to investigate the dynamics and power extraction of a Spar-buoy OWC. The numerical analysis shows that the channel wall can improve the capture breadth for both regular and irregular waves. Based on a fully nonlinear 3D CFD model, Elhanafi et al. [24] used the RAN-VOF approach to study the effects of wave

* Corresponding author at: State Key Laboratory of Coastal and Offshore Engineering, Dalian University of Technology, Dalian 116024, China.
E-mail address: chongweizhang@dlut.edu.cn (C. Zhang).

https://doi.org/10.1016/j.apor.2018.06.016
Received 23 March 2018; Received in revised form 25 May 2018; Accepted 20 June 2018
Available online 29 June 2018
0141-1187/ © 2018 The Authors. Published by Elsevier Ltd. This is an open access article under the CC BY license (http://creativecommons.org/licenses/BY/4.0/).

Nomenclature

Notation

A	Wave amplitude
A_{mn}	Constant coefficient
b	Breadth of the outer chamber
B_{mn}	Constant coefficient
$\widetilde{B}$	Damping coefficient
c	Sound velocity
C_{mn}	Constant coefficient
C_g	Group velocity
$\widetilde{C}$	Added mass coefficient
d	Draught of the cylinder
d_1	Draught of Shell-1
d_2	Draught of Shell-2
d_3	Immersion depth
d_{wall}	Shell thickness
D	Turbine diameter
D_{mn}	Constant coefficient
E	Constant coefficient
E_{mn}	Constant coefficient
F_{mn}	Constant coefficient
g	Gravitational acceleration
h	Water depth
$H_m^{(1)}$	Hankel function of the first kind
I_m	Modified Bessel function of the first kind
J_m	Bessel function of the first kind
K	Empirical coefficient for turbine
K_m	Modified Bessel function of the second kind
K_{mn}	Constant coefficient
k	Incident wave number
m	Order in circumference direction
M	Truncation number
N	Speed of turbine rotation in r. p. m.
P	Air pressure
P_0	Amplitude of the pressure
μ	Time-averaged value of the power captured
q_0	Amplitude volume flux
q_D	Amplitude volume flux for diffraction problem
q_R	Amplitude volume flux for radiation problem
r	Radial coordinate
Re	Real part of a complex variable
R_1	Radius of solid cylinder
R_2	Inside radius of Shell-1
R_3	Outside radius of Shell-1 and radius of pedestal
R_4	Inside radius of Shell-2
R_5	Outside radius of Shell-2
S_B	Mean wet body surface
S_D	Seabed
S_F	External free surface
S_i	Internal free surface
S_{in}	Cross-section area of the inner surface
S_{out}	Cross-section area of the outer surface
t	Time
T	Height of pedestal
U_{mn}	Constant coefficient
V_0	Mean chamber volume
V_{mn}	Constant coefficient
W_{mn}	Constant coefficient
z	Vertical coordinate
ω	Angular frequency
ρ_a	Air density
χ	Turbine parameter
β	Air compressible coefficient
ρ	Water density
φ	Velocity potential
θ	Azimuthal coordinate
Ω	Mean fluid domain
σ_D	A switch for diffraction problem
σ_R	A switch for the radiation problem
δkh	Frequency bandwidth for $\xi = 0.3$
ε_m	Neumann symbol
ζ	Dimensionless air chamber volume
ξ	Power extraction efficiency

conditions, PTO damping and mooring line pre-tension on an offshore floating OWC-WEC. It was found that the PTO damping and surge motion of the OWC-WEC can improve the device efficiency over respective frequency zone. Crespo et al. [25] conducted three numerical experiments to simulate the hydrodynamics of a floating offshore OWC-WEC with the mesh-free code DualSPHysics. Elhanafi et al. [26] conducted a parametric study on the hydrodynamic performance of an offshore stationary OWC-WEC, and found that both the submergence ratio of asymmetric lips and the lip thickness have a significant impact on boarding the effective frequency bandwidth. Besides, some floating OWC-WECs have also been studied and tested in prototype such as Mighty Whale (110KW) in Japan [27], Oceanlinx MK3(2.5 MW) in Australia [11] and so on. Most of the above-mentioned studies just consider the single-chamber OWC-WECs. The single-chamber OWC-WECs can work efficiently, but only within a narrow frequency bandwidth.

Regarding random ocean waves in reality, broadening the effective frequency bandwidth of an OWC-WEC is of great importance for its adaption to variable ocean wave environment. Some studies indicate that it can be a practical option to broaden the effective frequency bandwidth of an OWC-WEC by properly introducing an additional chamber. For example, Rezanejad et al. [28,29] theoretically and numerically analyzed the hydrodynamic efficiency of a dual-chamber OWC-WEC placed over a stepped bottom, and found that the effective frequency bandwidth of the device was broadened significantly compared with the single-chamber case. He et al. [30] performed experiments for floating box-type breakwaters with dual pneumatic chambers, and also indicated that dual chambers can broaden the effective frequency bandwidth. Wang et al. [31] numerically studied the hydrodynamic efficiency of the land-based OWC-WEC and reported that a proper set-up of sub-chambers can increase the general hydrodynamic efficiency of the OWC-WEC. Ning et al. [32] further discussed the free surface elevation and the air pressure in chambers of the dual-chamber OWC-WEC. Nevertheless, the above-mentioned dual-chamber OWC-WECs are all two-dimensional models.

The air compressibility plays an important role in large-scale OWC-WEC simulations, both in numerical and experimental studies [33]. Based on the isentropic assumption, Sheng [34] developed an accepted semi-empirical model to investigate the thermodynamics of the air flow for OWC-WECs. Teixeira et al. [35] investigated the effect of the air compressibility by varying the height of the air chamber. The results show that the efficiency increases slightly as the chamber height decreases. Martin-Rivas and Mei [36] simulated a thin cylindrical OWC-WEC installed at the tip of the breakwater. It is concluded that the air compressibility can broaden the bandwidth of the extraction efficiency with a specific chamber volume. Elhanafi et al. [37] analyzed effects of the scaling and air compressibility on a three-dimensional offshore OWC-WEC. The maximum efficiency reduces 12% with the optimum PTO damping at full-scale air compressibility. The above investigations of air compressibility are concentrated on the optimum PTO damping.

In reality, the turbine damping or rotating speed varies in different wave conditions. However, studies of the relationship between chamber volume and PTO damping are still limited.

To overcome the above disadvantages, a three-dimensional dual-chamber OWC-WEC is put forward based on the previous design [38] (shown in Fig. 1(a)). The improvement is achieved by additionally introducing a concentric cylindrical shell, as shown in Fig. 1(b). Based on the linear potential theory, an analytical model is developed to analyze the hydrodynamic properties of the dual-chamber device. The analytical method has been popularly used for the preliminary research of the OWC-WECs, such as Martins-Rivas and Mei [39], Sarmento and Falcão [40], Konispoliatis and Mavrakos [41], and Zhu and Mitchell [42]. The primary goal of the present study is to investigate the free-surface elevation and energy conversion efficiency, including hydrodynamic effects of the air compressibility and turbine rotating speed for the proposed device.

The paper is organized as follows. Sections 2 describes the power take-off model and analytical solutions of the hydrodynamic problem. In Section 3, the convergence and accuracy of the model are verified. Then, effects of structural and environmental parameters, air compressibility and rotational turbine speed on the hydrodynamic efficiency of the OWC-WEC are studied systematically. Comparisons with the single-chamber OWC-WEC are also given. Conclusions are drawn in Section 4.

2. Mathematical model

As shown in Fig. 2, the submerged part of the proposed OWC-WEC can be considered as the combination of a solid cylinder with two concentric cylindrical shells. A floating pedestal is also introduced at the bottom of the structure to provide buoyancy, so that the proposed OWC-WEC can work in the deep water. The inner and out shells are named as Shell-1 and Shell-2 hereafter for short, respectively. Two chambers are formed between the solid cylinder and Shell-1, and between Shell-1 and Shell-2. The following symbols are used to represent the geometric parameters of the structure, i.e., T – height of pedestal, d – draught of the cylinder, d_1 – draught of Shell-1, d_2 – draught of Shell-2, d_3-immersion depth, R_1 – radius of solid cylinder, R_3 – radius of Shell-1, R_5 – radius of Shell-2, and R_3 – radius of pedestal. The radii of Shell-1 and pedestal are designed to be identical for convenience. The water depth is constant h.

2.1. Power take-off model

In this study, the structure is rigid and fixed in the water. The fluid is assumed to be inviscid, incompressible and flow-irrotational. A Cartesian coordinate system O-xyz is defined, with the origin O at the intersection of the cylinder axis and undisturbed free surface, z-axis pointing vertically upwards, and x-axis in the direction of incident waves.

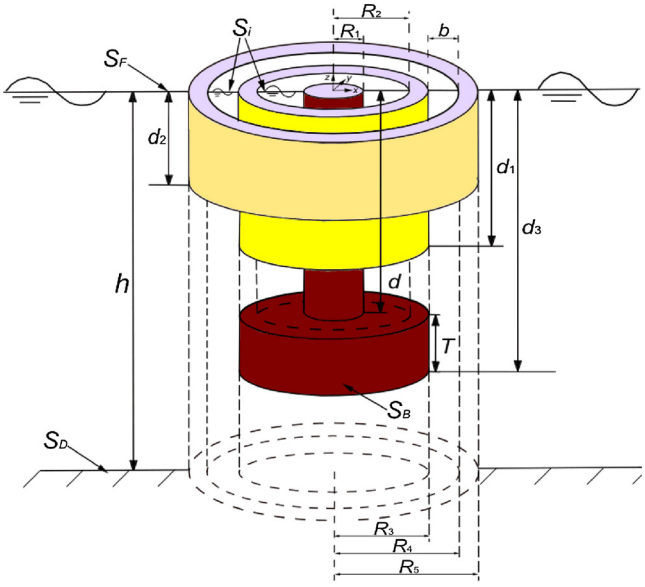

Fig. 2. Schematic of the dual-chamber OWC wave energy converter.

The air in the chamber is considered to be compressible and motion-isentropic (adiabatic process). Since the flow velocity of the air in the chamber is much slower than the speed of sound in air, the air pressure in the chamber can be considered uniform. The present study focuses on the steady state, so that all time-dependent variables in the problem are assumed to be harmonic. The air pressure P in the chamber has the following form

$$P = \mathrm{Re}[P_0 e^{-i\omega t}] \tag{1}$$

where ω is the wave angular frequency, t is the time, Re is the real part of a complex variable, P_0 is the complex amplitude of the pressure, and $i = \sqrt{-1}$. Referring to Sarmento and Falcao [40], the pressure difference across the turbine is proportional to the mass flux rate of the air, and the relationship between the air mass flux and the turbine characteristics can be expressed as

$$q_0 = \left(\frac{KD}{N\rho_a} - \frac{i\omega V_0}{c^2\rho_a}\right)P_0 \tag{2}$$

where q_0 is the amplitude volume flux, V_0 is the mean chamber volume, ρ_a is the air density, D is the diameter of the turbine rotor, N is the rate of turbine rotation in r. p. m., c is the speed of the sound in air, and K is an empirical coefficient depending on the design of turbines [36].

Based on the linear theory, the volume flux in the chamber is the sum of volume fluxes due to the wave radiation and diffraction. The

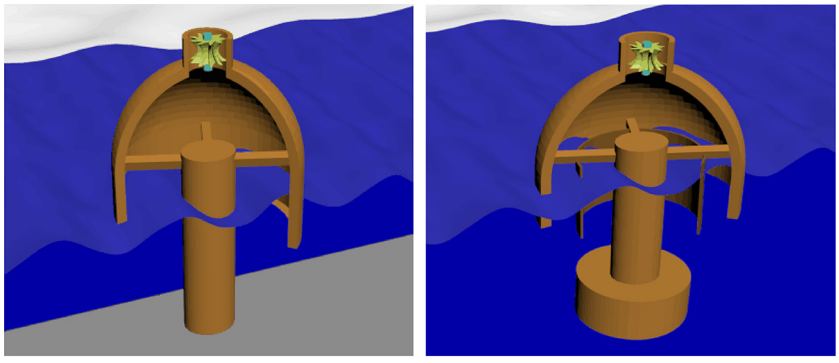

(a) (b)

Fig. 1. Concept of the (a) single-chamber and (b) dual-chamber OWC-WEC.

wave radiation occurs in the situation when the wave motion is purely caused by the air pressure oscillation in the chamber. The wave diffraction is due to the scattering of incident waves when the air pressures inside and outside the chamber are identical. Thus, the complex amplitude of the volume flux has two components

$$q_0 = q_D + P_0 q_R \tag{3}$$

where q_D and q_R are associated with the diffraction and radiation problems, respectively. For a radiation problem, an added mass coefficient $\widetilde{C}$ and a damping coefficient $\widetilde{B}$ can be obtained [43]. Complex amplitude of the volume flux q_R can be expressed as

$$q_R = -\widetilde{B} + i\widetilde{C} \tag{4}$$

By substituting Eqs. (3) and (4) into Eq. (2), the air pressure in the chamber can be expressed as follows

$$P_0 = \frac{q_D}{\left[\left(\frac{KD}{N\rho_a} + \widetilde{B}\right) - i\left(\widetilde{C} + \frac{\omega V_0}{c^2\rho_a}\right)\right]} \tag{5}$$

where q_D is solved from the wave diffraction problem, $\widetilde{B}$ and $\widetilde{C}$ can be obtained by solving the radiation problem with a unit forced pressure.

The time-averaged value of the power captured by the turbine, ζ is

$$\zeta = \frac{KD}{2N\rho_a}|P_a|^2 \tag{6}$$

The power extraction efficiency ξ can be calculated as [18]

$$\xi = \frac{k\zeta}{\rho g A C_g/2} = \frac{gkR_5}{\omega C_g}\frac{\chi\,|Q_D|^2}{(\chi + B)^2 + (\beta + C)^2} \tag{7}$$

where $Q_D = \omega q_D/(AR_5 g)$, $(B, C) = (\omega\rho\widetilde{B}, \omega\rho\widetilde{C})/R_5$, $\chi = \rho\omega KD/(N\rho_a R_5)$, and $\beta = V_0\omega^2\rho/(c_a^2 R_5\rho_a)$ are non-dimensional parameters. Here, χ characterizes the turbine, β represents the air compressibility, C_g is the group velocity of the incident wave, ρ denotes the water density, g is the gravitational acceleration and k is the incident wave number.

2.2. Solution of boundary value problems

Both the diffraction and radiation problems can be solved according to the potential-flow theory. The velocity potential φ whose gradient is the fluid velocity is used to describe the flow. For the steady state considered in this study, all time-dependent variables in the problem are assumed to be harmonic. The velocity potential is expressed as

$$\varphi(r, \theta, z, t) = \mathrm{Re}[\phi(r, \theta, z)e^{-i\omega t}] \tag{8}$$

where r, θ and z are radial, azimuthal and vertical coordinates in a cylindrical coordinate system, respectively, and ϕ is the spatial velocity potential. The linearized boundary value problem of ϕ is defined as follows:

$$\nabla^2\phi(r, \theta, z) = \frac{1}{r}\frac{\partial}{\partial r}\left(r\frac{\partial\phi}{\partial r}\right) + \frac{1}{r^2}\frac{\partial^2\phi}{\partial\theta^2} + \frac{\partial^2\phi}{\partial z^2} = 0, \quad in \quad \Omega \tag{9}$$

$$\frac{\partial\phi}{\partial n} = 0, \quad \text{on} \quad S_B \quad \text{and} \quad S_D \tag{10}$$

$$\frac{\partial\phi}{\partial z} - \frac{\omega^2}{g}\phi = \begin{cases} i\omega\sigma_R P_0/\rho g, & \text{on} \quad S_i \\ 0, & \text{on} \quad S_F \end{cases} \tag{11}$$

where Ω is the mean fluid domain, S_B is the mean wet body surface, S_F is the external free surface, S_i is the internal free surface, S_D is the seabed, and $\partial/\partial n$ denotes the normal derivative of a variable on the body surface. For the completeness, a radiation condition is also required on the open boundary of the fluid domain. It should be highlighted that σ_R is used as a switch between the radiation and diffraction problems. For the radiation problem, $\sigma_R = 1$ is set and the pressure in the chamber is $P_0 = 1$. For the diffraction problem, $\sigma_R = 0$ is set.

In order to obtain an analytical solution of the above boundary value problem, the fluid domain is divided into six subdomains as depicted in Fig. 3. It should be noted that Shell-1 and Shell-2 are given a thickness here for an extension of the model. Internal surfaces of Shell-1 and Shell-2 have radiuses of R_2 and R_4, respectively. To be specific, subdomain Ω_1 is defined by $r \geq R_5$ and $-h \leq z \leq 0$, Ω_2 is by $r \leq R_3$ and $-h \leq z \leq -d_3$, Ω_3 is by $R_1 \leq r \leq R_2$ and $-d \leq z \leq 0$, Ω_4 is by $R_2 \leq r \leq R_3$ and $-d \leq z \leq d_1$, Ω_5 is by $R_4 \leq r \leq R_5$ and $-h \leq z \leq d_2$, and Ω_6 is by $R_3 \leq r \leq R_4$ and $-h \leq z \leq 0$. The superscript *(i)* is used to denote a variable in subdomain Ω_i. According to the method of separation of variables, the expression of $\phi^{(i)}$ can be constructed as follows:

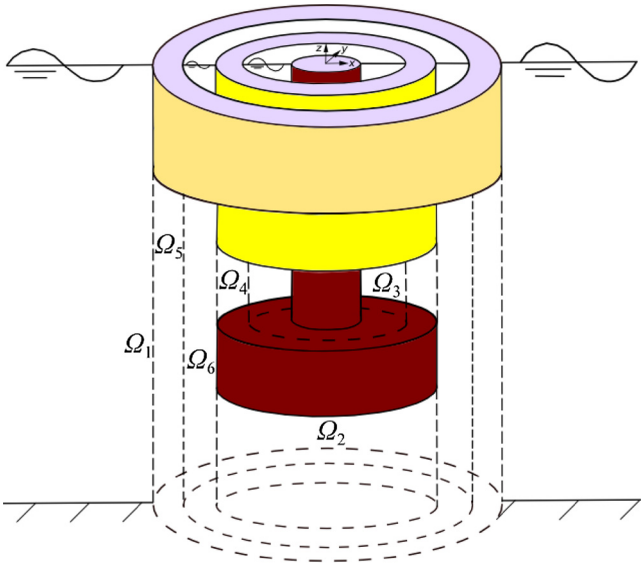

Fig. 3. Six subdomains of the OWC-WEC analytical model.

$$\phi^{(1)}(r, \theta, z) = \sigma_D E\sum_{m=0}^{\infty}\varepsilon_m i^m\cos(m\theta)J_m(k_0^{(1)}r)Z_0^{(1)}(z) + E\sum_{m=0}^{\infty}\varepsilon_m i^m\cos(m\theta)\left[\sum_{n=0}^{\infty}A_{mn}P_{mn}^{(1)}(k_n^{(1)}r)Z_n^{(1)}(z)\right] \tag{12}$$

$$\phi^{(2)}(r, \theta, z) = \sum_{m=0}^{\infty}\cos(m\theta)\sum_{n=0}^{\infty}[B_{mn}P_{mn}^{(2)}(k_n^{(2)}r)]Z_n^{(2)}(z) \tag{13}$$

$$\phi^{(3)}(r, \theta, z) = \sum_{m=0}^{\infty}\cos(m\theta)\sum_{n=0}^{\infty}[C_{mn}P_{mn}^{(3)}(k_n^{(3)}r) + D_{mn}Q_{mn}^{(3)}(k_n^{(3)}r)]Z_n^{(3)}(z) - \frac{i\sigma_R P_0}{\rho\omega} \tag{14}$$

$$\phi^{(4)}(r, \theta, z) = \sum_{m=0}^{\infty}\cos(m\theta)\sum_{n=0}^{\infty}[E_{mn}P_{mn}^{(4)}(k_n^{(4)}r) + F_{mn}Q_{mn}^{(4)}(k_n^{(4)}r)]Z_n^{(4)}(z) \tag{15}$$

$$\phi^{(5)}(r, \theta, z) = \sum_{m=0}^{\infty}\cos(m\theta)\sum_{n=0}^{\infty}[U_{mn}P_{mn}^{(5)}(k_n^{(5)}r) + V_{mn}Q_{mn}^{(5)}(k_n^{(5)}r)]Z_n^{(5)}(z) \tag{16}$$

$$\phi^{(6)}(r, \theta, z) = \sum_{m=0}^{\infty}\cos(m\theta)\sum_{n=0}^{\infty}[K_{mn}P_{mn}^{(6)}(k_n^{(6)}r) + W_{mn}Q_{mn}^{(6)}(k_n^{(6)}r)]Z_n^{(6)}(z) - \frac{i\sigma_R P_0}{\rho\omega} \tag{17}$$

where A_{mn}, B_{mn}, C_{mn}, D_{mn}, E_{mn}, F_{mn}, U_{mn}, V_{mn}, K_{mn}, and W_{mn} are the constant coefficients, $E = -igA/\omega\cosh kh$ is a constant with A as wave amplitude, $\varepsilon_m = \{1, for m = 0; 2, for m \geq 1\}$ is the Neumann symbol, and $\sigma_D = 1 - \sigma_R$ is a switch to the diffraction problem. $k_n^{(1)}$, $k_n^{(2)}$, $k_n^{(3)}$, $k_n^{(4)}$, $k_n^{(5)}$ and $k_n^{(6)}$ are the positive real roots of the following equations

$$\omega^2/g = \begin{cases} k_0^{(1)} \tanh k_0^{(1)} h, \text{ for} n = 0 \\ -k_n^{(1)} \tan k_n^{(1)} h, \text{ for} n \geq 1 \end{cases} \tag{18}$$

$$k_n^{(2)} = n\pi/(h - d_3) \tag{19}$$

$$\omega^2/g = \begin{cases} k_0^{(3)} \tanh k_0^{(3)} d, \text{ for} n = 0 \\ -k_n^{(3)} \tan k_n^{(3)} d, \text{ for} n \geq 1 \end{cases} \tag{20}$$

$$k_n^{(4)} = n\pi/(d - d_1) \tag{21}$$

$$k_n^{(5)} = n\pi/(h - d_2) \tag{22}$$

$$\omega^2/g = \begin{cases} k_0^{(6)} \tanh k_0^{(6)} h, \text{ for} n = 0 \\ -k_n^{(6)} \tan k_n^{(6)} h, \text{ for} n \geq 1 \end{cases} \tag{23}$$

Expressions of $P_{mn}(k_n r)$ and $Q_{mn}(k_n r)$ are given as

$$P_{mn}^{(1)}(r) = \{H_m^{(1)}(k_0^{(1)} r),\ n = 0;\ K_m(k_n^{(1)} r),\ n \geq 1\} \tag{24}$$

$$P_{mn}^{(2)}(r) = \{r^m,\ n = 0;\ I_m(k_n^{(2)} r),\ n \geq 1\} \tag{25}$$

$$P_{mn}^{(3)} = \{J_m(k_0^{(3)} r),\ n = 0;\ I_m(k_n^{(3)} r),\ n \geq 1\} \tag{26}$$

$$P_{mn}^{(4)} = \{r^m,\ n = 0;\ I_m(k_n^{(4)} r),\ n \geq 1\} \tag{27}$$

$$P_{mn}^{(5)} = \{r^m,\ n = 0;\ I_m(k_n^{(5)} r),\ n \geq 1\} \tag{28}$$

$$P_{mn}^{(6)} = \{J_m(k_0^{(6)} r),\ n = 0;\ I_m(k_n^{(6)} r),\ n \geq 1\} \tag{29}$$

$$Q_{mn}^{(3)} = \{H_m^{(1)}(k_0^{(3)} r),\ n = 0;\quad K_m(k_n^{(3)} r),\ n \geq 1\} \tag{30}$$

$$Q_{mn}^{(4)} = \{\ln(r),\ m = 0,\ n = 0;\quad r^{-m},\ m \neq 0,\ n = 0;\quad K_m(k_n^{(4)} r),\ n \geq 1\} \tag{31}$$

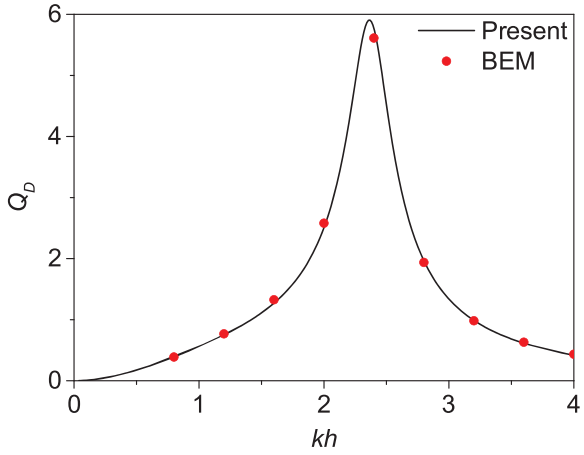

Fig. 5. Comparisons of Q_D between present model and BEM model.

$$Q_{mn}^{(5)} = \{\ln(r),\ m = 0,\ n = 0;\quad r^{-m},\ m \neq 0,\ n = 0;\quad K_m(k_n^{(5)} r),\ n \geq 1\} \tag{32}$$

$$Q_{mn}^{(6)} = \{H_m^{(1)}(k_0^{(6)} r),\ n = 0;\quad K_m(k_n^{(6)} r),\ n \geq 1\} \tag{33}$$

Here, J_m is the Bessel function of the first kind, $H_m^{(1)}$ is the Hankel function of the first kind, I_m is the modified Bessel function of the first kind, and K_m is the modified Bessel function of the second kind, all of order m. According to the boundary conditions, the following vertical eigenfunctions can be obtained in each domain

$$Z_n^{(1)}(z) = \begin{cases} \cosh k_0^{(1)}(z + h), \text{ for} n = 0 \\ \cos k_n^{(1)}(z + h), \text{ for} n \geq 1 \end{cases} \tag{((34))}$$

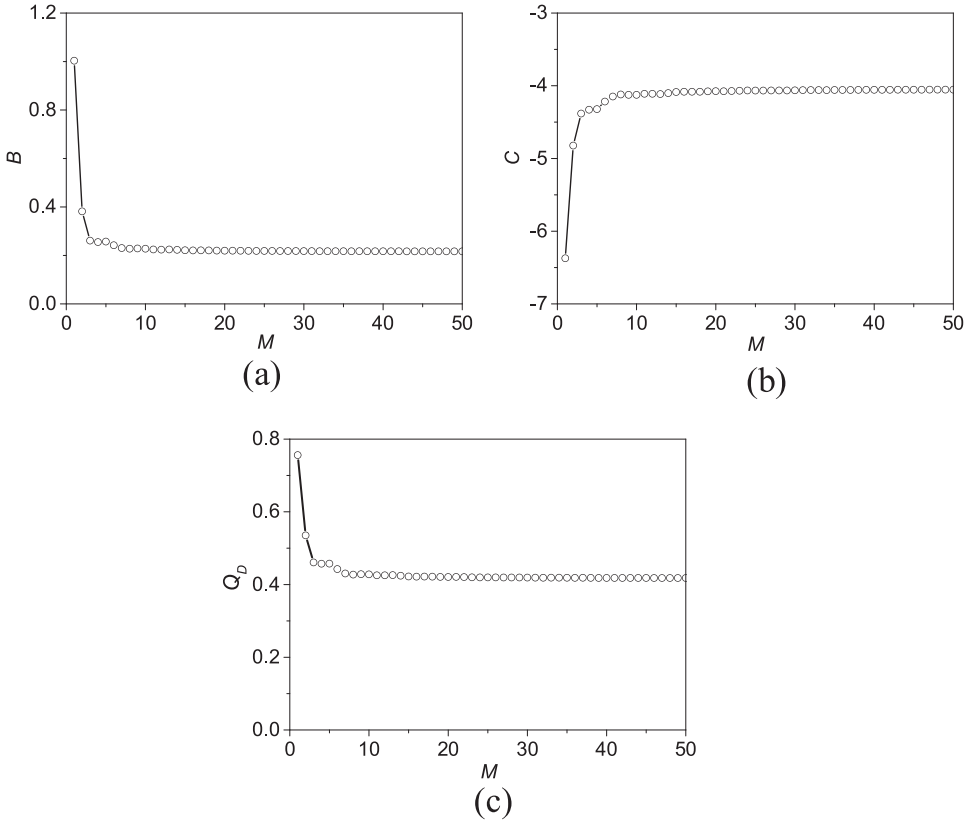

Fig. 4. Convergent study with respect to M, for (a) B, (b) C, (c) Q_D.

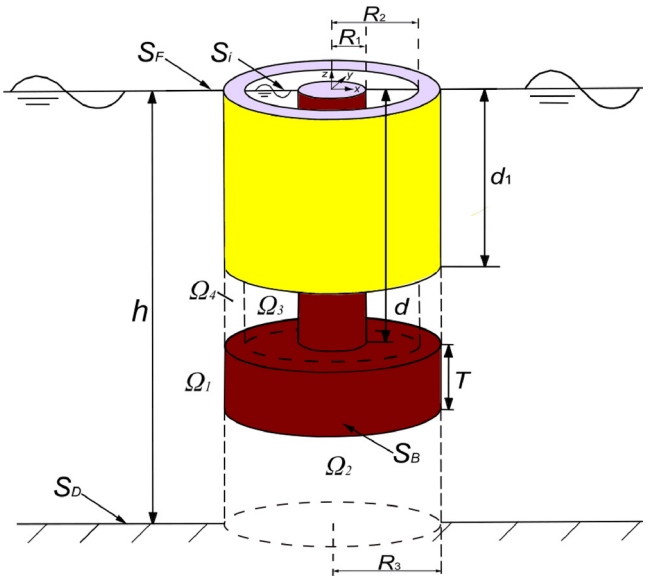

Fig. 6. Schematic of the single-chamber OWC-WEC.

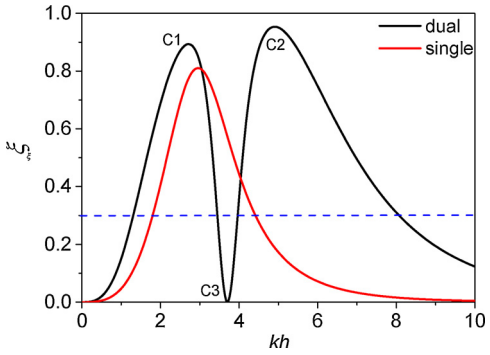

Fig. 7. Distribution of efficiency ξ with kh between single- and dual-chamber OWC-WECs.

$$Z_n^{(2)}(z) = \begin{cases} \sqrt{2}/2, \text{ for} n = 0 \\ \cos k_n^{(2)}(z+h), \text{ for} n \geq 1 \end{cases} \tag{35}$$

$$Z_n^{(3)}(z) = \begin{cases} \cosh k_0^{(3)}(z+d), \text{ for} n = 0 \\ \cos k_n^{(3)}(z+d), \text{ for} n \geq 1 \end{cases} \tag{36}$$

$$Z_n^{(4)}(z) = \begin{cases} \sqrt{2}/2, \text{ for} n = 0 \\ \cos k_n^{(4)}(z+d), \text{ for} n \geq 1 \end{cases} \tag{37}$$

$$Z_n^{(5)}(z) = \begin{cases} \sqrt{2}/2, \text{ for} n = 0 \\ \cos k_n^{(5)}(z+h), \text{ for} n \geq 1 \end{cases} \tag{38}$$

$$Z_n^{(6)}(z) = \begin{cases} \cosh k_0^{(6)}(z+h), \text{ for} n = 0 \\ \cos k_n^{(6)}(z+h), \text{ for} n \geq 1 \end{cases} \tag{39}$$

The following matching conditions are applied on the interfaces of adjacent subdomains, to guarantee the continuity of the velocity potential and velocity in the fluid domain:

$$\phi^{(1)} = \phi^{(5)}, \text{ for} r = R_5 \text{and} -h \leq z \leq -d_2 \tag{40}$$

$$\phi^{(5)} = \phi^{(6)}, \text{ for} r = R_4 \text{and} -h \leq z \leq -d_2 \tag{41}$$

$$\phi^{(6)} = \phi^{(4)}, \text{ for} r = R_3 \text{and} -d \leq z \leq -d_1 \tag{42}$$

$$\phi^{(6)} = \phi^{(2)}, \text{ for} r = R_3 \text{and} -h \leq z \leq -d_3 \tag{43}$$

$$\phi^{(3)} = \phi^{(4)}, \text{ for} r = R_2 \text{and} -d \leq z \leq -d_1 \tag{44}$$

$$\partial\phi^{(1)}/\partial r = \begin{cases} 0, \text{ for} r = R_5 \text{and} -d_2 \leq z \leq 0 \\ \partial\phi^{(5)}/\partial r, \text{ for} r = R_5 \text{and} -h \leq z \leq -d_2 \end{cases} \tag{45}$$

$$\partial\phi^{(6)}/\partial r = \begin{cases} 0, \text{ for} r = R_4 \text{and} -d_2 \leq z \leq 0 \\ \partial\phi^{(5)}/\partial r, \text{ for} r = R_4 \text{and} -h \leq z \leq -d_2 \end{cases} \tag{46}$$

$$\partial\phi^{(6)}/\partial r = \begin{cases} \partial\phi^{(4)}/\partial r, \text{ for} r = R_3 \text{and} -d \leq z \leq -d_1 \\ \partial\phi^{(2)}/\partial r, \text{ for} r = R_3 \text{and} -h \leq z \leq -d_3 \end{cases} \tag{47}$$

$$\partial\phi^{(3)}/\partial r = \begin{cases} 0, \text{ for} r = R_2 \text{and} -d_1 \leq z \leq 0 \\ \partial\phi^{(4)}/\partial r, \text{ for} r = R_2 \text{and} -d \leq z \leq -d_1 \end{cases} \tag{48}$$

$$\partial\phi^{(3)}/\partial r = 0, \text{ for} r = R_1 \text{and} -d \leq z \leq 0 \tag{49}$$

By substituting the general solutions of ϕ into the above conditions and taking advantage of the orthogonal relationship of vertical eigenfunctions, the following linear system of equations can be obtained

$$\sum_{n=0}^{\infty} A_{mn}[E\varepsilon_m i^m P_{mn}^{(1)}(R_5)a_{nl}^{(1)}] - \sum_{n=0}^{\infty} U_{mn}[P_{mn}^{(5)}(R_5)b_{nl}^{(1)}] - \sum_{n=0}^{\infty} V_{mn}[Q_{mn}^{(5)}(R_5)b_{nl}^{(1)}] = -\sigma_D E\varepsilon_m i^m J_m(k_0^{(1)}R_5)a_{0l}^{(1)} \tag{50}$$

$$\sum_{n=0}^{\infty} K_{mn}[P_{mn}^{(6)}(R_4)a_{nl}^{(2)}] + \sum_{n=0}^{\infty} W_{mn}[Q_{mn}^{(6)}(R_4)a_{nl}^{(2)}] - \sum_{n=0}^{\infty} U_{mn}[P_{mn}^{(5)}(R_4)b_{nl}^{(2)}] - \sum_{n=0}^{\infty} V_{mn}[Q_{mn}^{(5)}(R_4)b_{nl}^{(2)}] = c_{0l}^{(2)} \tag{51}$$

$$\sum_{n=0}^{\infty} K_{mn}[P_{mn}^{(6)}(R_3)a_{nl}^{(3)}] + \sum_{n=0}^{\infty} W_{mn}[Q_{mn}^{(6)}(R_3)a_{nl}^{(3)}] - \sum_{n=0}^{\infty} E_{mn}[P_{mn}^{(4)}(R_3)b_{nl}^{(3)}] - \sum_{n=0}^{\infty} F_{mn}[Q_{mn}^{(4)}(R_3)b_{nl}^{(3)}] = c_{0l}^{(3)} \tag{52}$$

$$\sum_{n=0}^{\infty} K_{mn}[P_{mn}^{(6)}(R_3)a_{nl}^{(4)}] + \sum_{n=0}^{\infty} W_{mn}[Q_{mn}^{(6)}(R_3)a_{nl}^{(4)}] - \sum_{n=0}^{\infty} B_{mn}[P_{mn}^{(2)}(R_3)b_{nl}^{(4)}] = c_{0l}^{(4)} \tag{53}$$

$$\sum_{n=0}^{\infty} E_{mn}[P_{mn}^{(4)}(R_2)a_{nl}^{(5)}] + \sum_{n=0}^{\infty} F_{mn}[Q_{mn}^{(4)}(R_2)a_{nl}^{(5)}] - \sum_{n=0}^{\infty} C_{mn}[P_{mn}^{(3)}(R_2)b_{nl}^{(5)}] - \sum_{n=0}^{\infty} D_{mn}[Q_{mn}^{(3)}(R_2)b_{nl}^{(5)}] = c_{0l}^{(5)} \tag{54}$$

$$\sum_{n=0}^{\infty} A_{mn}\left[E\varepsilon_m i^m \frac{dP_{mn}^{(1)}(R_5)}{dr}a_{nl}^{(6)}\right] - \sum_{n=0}^{\infty} U_{mn}\left[\frac{dP_{mn}^{(5)}(R_5)}{dr}b_{nl}^{(6)}\right] - \sum_{n=0}^{\infty} V_{mn}\left[\frac{dQ_{mn}^{(5)}(R_5)}{dr}b_{nl}^{(6)}\right] = -\sigma_D E\varepsilon_m i^m k_0^{(1)}\frac{dJ_m(k_0^{(1)}R_5)}{dr}a_{00}^{(6)} \tag{55}$$

$$\sum_{n=0}^{\infty} K_{mn}\left[\frac{dP_{mn}^{(6)}(R_4)}{dr}a_{nl}^{(7)}\right] + \sum_{n=0}^{\infty} W_{mn}\left[\frac{dQ_{mn}^{(6)}(R_4)}{dr}a_{nl}^{(7)}\right] - \sum_{n=0}^{\infty} U_{mn}\left[\frac{dP_{mn}^{(5)}(R_4)}{dr}b_{nl}^{(7)}\right] - \sum_{n=0}^{\infty} V_{mn}\left[\frac{dQ_{mn}^{(5)}(R_4)}{dr}b_{nl}^{(7)}\right] = 0 \tag{56}$$

$$\sum_{n=0}^{\infty} K_{mn}\left[\frac{dP_{mn}^{(6)}(R_3)}{dr}a_{nl}^{(8)}\right] + \sum_{n=0}^{\infty} W_{mn}\left[\frac{dQ_{mn}^{(6)}(R_3)}{dr}a_{nl}^{(8)}\right] - \sum_{n=0}^{\infty} B_{mn}\left[\frac{dP_{mn}^{(2)}(R_3)}{dr}b_{nl}^{(8)}\right] - \sum_{n=0}^{\infty} E_{mn}\left[\frac{dP_{mn}^{(4)}(R_3)}{dr}c_{nl}^{(8)}\right] - \sum_{n=0}^{\infty} F_{mn}\left[\frac{dQ_{mn}^{(4)}(R_3)}{dr}c_{nl}^{(8)}\right] = 0 \tag{57}$$

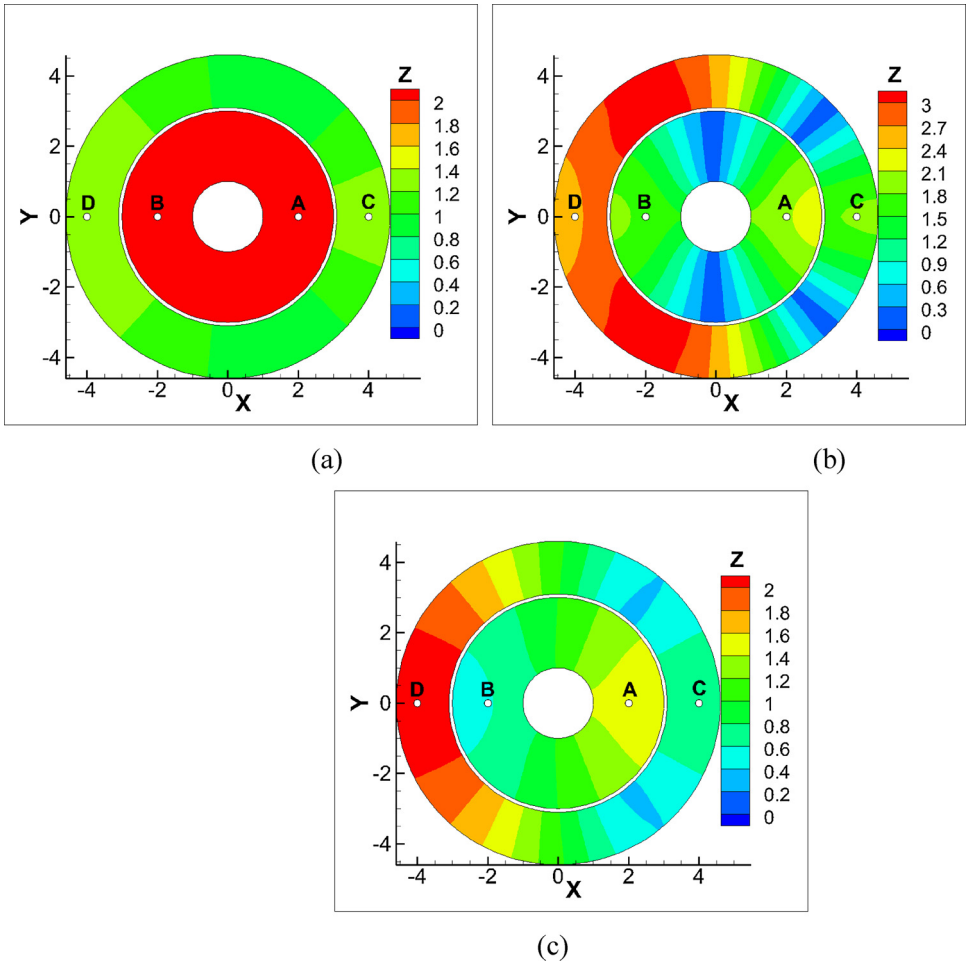

Fig. 8. Free-surface in chambers at (a) C1, (b) C2, and (c) C3 of dual-chamber OWC-WEC (For interpretation of the references to color in text, the reader is referred to the web version of this article).

$$\sum_{n=0}^{\infty} C_{mn}\left[\frac{dP_{mn}^{(3)}(R_2)}{dr}a_{nl}^{(9)}\right] + \sum_{n=0}^{\infty} D_{mn}\left[\frac{dQ_{mn}^{(3)}(R_2)}{dr}a_{nl}^{(9)}\right] - \sum_{n=0}^{\infty} E_{mn}\left[\frac{dP_{mn}^{(4)}(R_2)}{dr}b_{nl}^{(9)}\right] - \sum_{n=0}^{\infty} F_{mn}\left[\frac{dQ_{mn}^{(4)}(R_2)}{dr}b_{nl}^{(9)}\right] = 0 \tag{58}$$

$$\sum_{n=0}^{\infty} C_{mn}\left[\frac{dP_{mn}^{(3)}(R_1)}{dr}a_{nl}^{(10)}\right] - \sum_{n=0}^{\infty} D_{mn}\left[\frac{dQ_{mn}^{(3)}(R_1)}{dr}b_{nl}^{(10)}\right] = 0 \tag{59}$$

with coefficients expressed as

$$\begin{aligned}
&a_{nl}^{(1)} = a_{nl}^{(2)} = \int_{-h}^{-d_2} Z_n^{(1)} Z_l^{(5)} dz; \quad b_{nl}^{(1)} = b_{nl}^{(2)} = \int_{-h}^{-d_2} Z_n^{(5)} Z_l^{(5)} dz;\\
&c_{0l}^{(2)} = \sigma_R \int_{-h}^{-d_2} iP_0/\rho\omega Z_l^{(5)} dz; \quad a_{nl}^{(3)} = \int_{-d}^{-d_1} Z_n^{(6)} Z_l^{(4)} dz; \quad b_{nl}^{(3)} = \int_{-d}^{-d_1} Z_n^{(4)} Z_l^{(4)} dz;\\
&c_{0l}^{(3)} = \sigma_R \int_{-d}^{-d_1} iP_0/\rho\omega Z_l^{(4)} dz; \quad a_{nl}^{(4)} = \int_{-h}^{-d_3} Z_n^{(6)} Z_l^{(2)} dz; \quad b_{nl}^{(4)} = \int_{-h}^{-d_3} Z_n^{(2)} Z_l^{(2)} dz;\\
&c_{0l}^{(4)} = \sigma_R \int_{-h}^{-d_3} iP_0/\rho\omega Z_l^{(2)} dz; \quad a_{nl}^{(5)} = \int_{-d}^{-d_1} Z_n^{(4)} Z_l^{(4)} dz; \quad b_{nl}^{(5)} = \int_{-d}^{-d_1} Z_n^{(3)} Z_l^{(4)} dz;\\
&c_{0l}^{(5)} = \sigma_R \int_{-d}^{-d_1} -iP_0/\rho\omega Z_l^{(4)} dz; \quad a_{nl}^{(6)} = a_{nl}^{(7)} = \int_{-h}^{0} Z_n^{(1)} Z_l^{(1)} dz;\\
&b_{nl}^{(6)} = b_{nl}^{(7)} = \int_{-h}^{-d_2} Z_n^{(5)} Z_l^{(1)} dz; \quad a_{nl}^{(8)} = \int_{-h}^{0} Z_n^{(6)} Z_l^{(6)} dz; \quad b_{nl}^{(8)} = \int_{-h}^{-d_3} Z_n^{(2)} Z_l^{(6)} dz;\\
&c_{nl}^{(8)} = \int_{-d}^{-d_1} Z_n^{(4)} Z_l^{(6)} dz; \quad a_{nl}^{(9)} = \int_{-d}^{0} Z_n^{(3)} Z_l^{(3)} dz; \quad b_{nl}^{(9)} = \int_{-d}^{-d_1} Z_n^{(4)} Z_l^{(3)} dz;\\
&a_{nl}^{(10)} = b_{nl}^{(10)}
\end{aligned} \tag{60}$$

By letting $m = 0 \sim M$, $l = 0 \sim M$ and $n = 0 \sim M$ in the eigen-function expansions, $(M + 1)$ systems of equations can be obtained. Each system of equations has $10 \times (M + 1)$ equations. For a certain m, the linear equations can be assembled as

$$[G(m)]\mathbf{X} = \mathbf{T} \tag{61}$$

with

$$\mathbf{X} = [A_{mn}, B_{mn}, C_{mn}, D_{mn}, E_{mn}, F_{mn}, U_{mn}, V_{mn}, K_{mn}, W_{mn}]^T \quad \text{for } n = 0,\ 1,\ \ldots, M \tag{62}$$

Once the coefficients A_{mn}, B_{mn}, C_{mn}, D_{mn}, E_{mn}, F_{mn}, U_{mn}, V_{mn}, K_{mn}, and W_{mn} are known, the velocity potential in each domain can be obtained based on Eqs. (50)–(59). LU factorization method is used to solve the linear equations. The complex amplitude of volume flux can be calculated by the free-surface integration

$$q_D = \iint_{S_{in}} \frac{\partial \phi_3}{\partial z} ds + \iint_{S_{out}} \frac{\partial \phi_6}{\partial z} ds \tag{63}$$

for wave diffraction problem, and

$$q_R = \iint_{S_{in}} \frac{\partial \phi_3}{\partial z} ds + \iint_{S_{out}} \frac{\partial \phi_6}{\partial z} ds \tag{64}$$

for wave radiation problem. S_{in} and S_{out} are the cross-section area of the free surface in the inner and outer chamber, respectively.

3. Results and discussion

3.1. Convergent and accurate tests

The convergence of the results with respect to the truncation number M in Eqs. (50)–(59) is firstly tested. In the first case, the parameters are set as $R_1/h = 0.125$, $R_2/h = 0.25$, $R_3/h = 0.375$, $R_4/h = 0.5$, $R_5/h = 0.625$, $d_1/h = 0.125$, $d_2/h = 0.25$, $d_3/h = 0.5$, $d/$

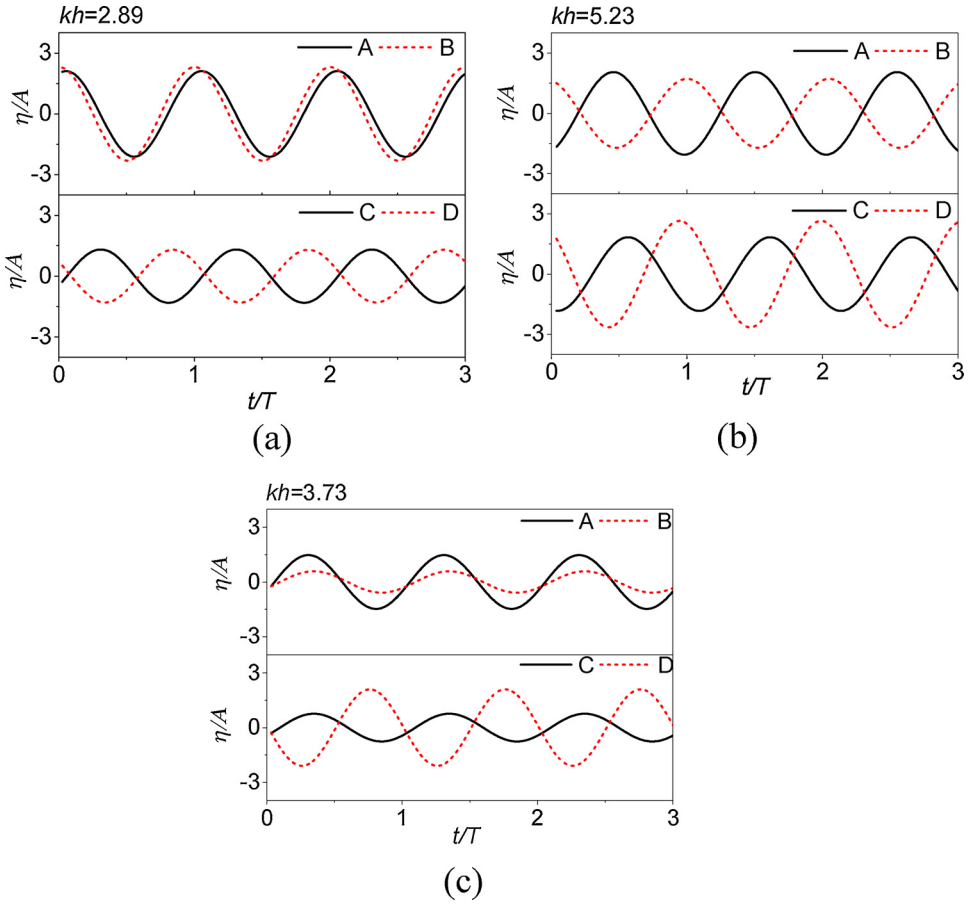

Fig. 9. Time series of free-surface elevation at test positions in the chamber, at the condition of dual-chamber OWC-WEC for (a) C1 (b) C2 (c) C3.

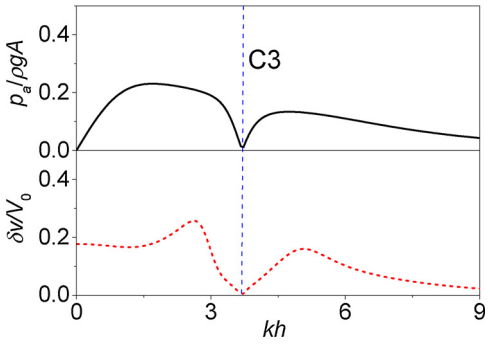

Fig. 10. Distribution of the air pressure and volume flux in the chamber with *kh*.

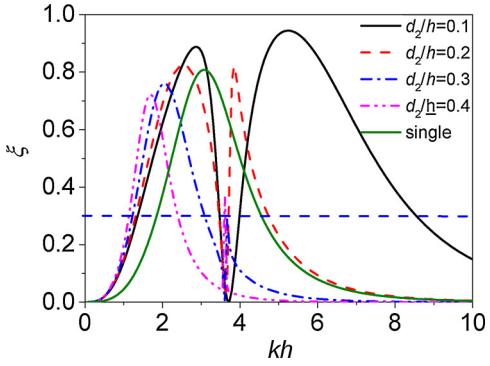

Fig. 11. Distribution of hydrodynamic efficiency for different draught of Shell-2 d_2 on the efficiency ξ.

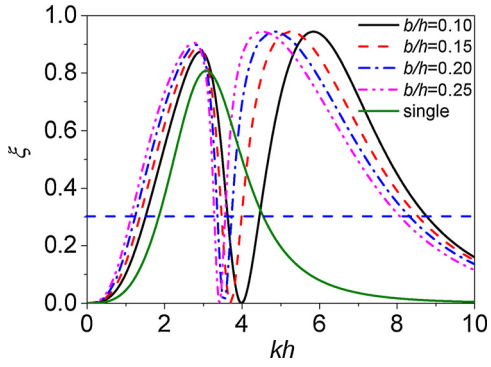

Fig. 12. Distribution of hydrodynamic efficiency for different breadth of the outer chamber b on the efficiency ξ.

$h = 0.375$ and $kh = 4.0$. Fig. 4 shows the obtained non-dimensional value of the added mass coefficient B, damping coefficient C, and volume flux Q_D with different M. It can be seen that the analytical convergence can be obtained as $M \geq 20$. Similar convergence can also be realized for other cases with the same value of M.

Then, the accuracy of the present solutions is examined. A higher-order boundary element method (BEM) [44] is applied to solve the diffraction problem with the same parameters as the above. Fig. 5 shows comparisons of the non-dimensional variable Q_D by the present model and the results of the BEM with different incident wave number. From these comparisons, the analytical results given by the two methods have a good agreement, and it can be taken as the validation of the present method.

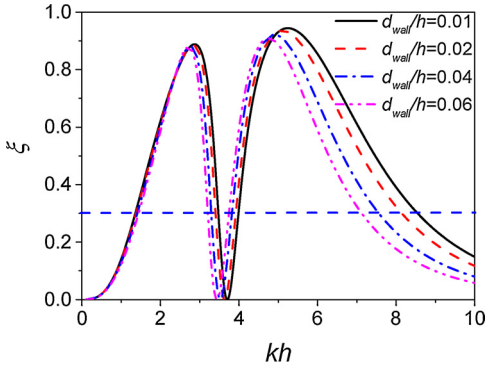

Fig. 13. Distribution of hydrodynamic efficiency for different shell thickness d_{wall} on the efficiency ξ.

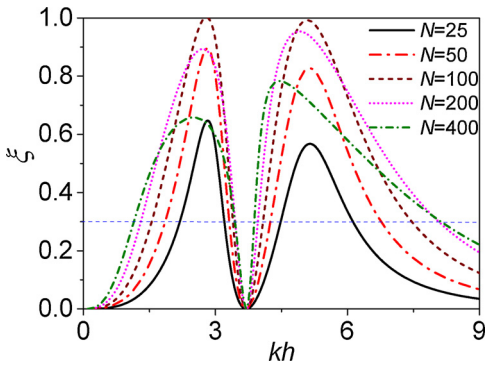

Fig. 14. Distribution of hydrodynamic efficiency for different turbine rotational speed N on the efficiency ξ.

3.2. Hydrodynamic performance of dual-chamber OWC-WEC

Effect of dual chambers on the power extraction efficiency ξ is firstly studied, through a comparison with the single-chamber model shown in Fig. 6. Geometric parameters of the single-chamber OWC-WEC are set as follows, $d_1/h = 0.2$, $T/h = 0.1$, $d/h = 0.5$, $(R_2 - R_1)/h = 0.2$ and $V_0 = \pi d R_5^2$. A Shell-2 with the radius $R_5/h = 0.35$ and draught $d_2/h = 0.1$ is installed external to the single-chamber OWC-WEC, forming the dual-chamber model. The shell thickness has the value $d_{wall}/h = 0.01$. The remaining parameters are set as $K = 0.5$, $N = 200$ r.p.m, $h = 10$ m, $A/h = 0.1$ and $\rho/\rho_a = 1023$, where the density of water is $\rho = 1023 kg/m^3$, and the density of air is $\rho_a = 1 kg/m^3$. Fig. 7 shows the comparison of the efficiency spectra between the single- and dual-chamber OWC-WECs with dimensionless wave number kh. A dashed line at $\xi = 0.3$ is marked in the figure to depict the effective frequency bandwidth (i.e., the part for $\xi \geq 0.3$). It can be seen that the effective frequency bandwidth of the dual-chamber case is about three times as large as that of the single-chamber case. Besides, the maximum efficiency of the dual-chamber OWC-WEC is about 8% greater than that of the single-chamber model. Thus, the dual-chamber OWC-WEC is superior to the corresponding single-chamber model in both the effective frequency bandwidth and the maximum hydrodynamic efficiency.

Then, the efficiency spectrum of the dual-chamber OWC-WEC in Fig. 7 is analyzed in detail. It can be seen that there exist two peak efficiencies of the dual-chamber OWC-WEC, unlike the single-peak efficiency of the single-chamber case. In the figure, we used C1 at $kh = 2.89$ and C2 at $kh = 5.23$ to denote the peak points and C3 at $kh = 3.73$ for the trough point. It is noted that the efficiency is null at C3. Around C3, a narrow frequency bandwidth with $\xi \leq 0.3$ occurs, as a 'blind spot' for the energy capture of the dual-chamber OWC-WEC device. However, the frequency bandwidth around C3 can be minimized through a modification of geometric parameters, which can be found in later results. Fig. 8 depicts the distribution of the surface oscillating amplitude in the chambers corresponding to C1, C2 and C3 conditions, respectively. An inner annulus free surface between the cylinder and Shell-1, and an outer annulus free surface between Shell-1 and Shell-2 are formed. Fig. 8(a) shows that the wave amplitude of the free surface is the same in the inner chamber, in which the wave amplitude is larger than those in the outer chamber. That means the inner chamber can make more contribution to the compressed air. In Fig. 8(b), the distribution of the inner free surface amplitude at C2 is nearly symmetrical about the cylinder, but the outer free surface oscillates more greatly. It is due to the wave reflection from Shell-1 that leads to larger wave amplitude in the red area of the outer chamber. Fig. 8(c) depicts the free surface profile of the two chambers at the C3 condition which will be further analyzed in the following section.

To make further analysis of the free surface movement, four points A(2,0,0), B(−2,0,0), C(4,0,0) and D(−4,0,0) are chosen on the chamber free surface. Time series of the free surface elevation at these points are shown in Fig. 9. Fig. 9(a) considers the dual-chamber OWC-WEC at C1. It can be seen that wave elevations at A and B in the inner chamber are almost in phase and with the similar amplitude, as a feature of the piston-type oscillation. However, the wave elevation histories at C and D are anti-phase, suggesting a sloshing mode that contributes little volume flux. Thus, it is the inner chamber that makes the major contribution to the hydrodynamic efficiency at the C1 condition. Fig. 9(b) shows the results at C2. It is found that the free-surface motions at A and B are nearly anti-phase with similar amplitudes, suggesting a sloshing-type free-surface motion. The free-surface histories at C and D are out of phase but not anti-phase. The free surface motion in the outer chamber includes the contribution of wave reflection from Shell-1, which leads to greater motion amplitude at D than that at C. Thus, the wave oscillation in the outer chamber makes the major contribution to the hydrodynamic efficiency of the dual-chamber OWC-WEC at the C2 condition. Fig. 9(c) shows the free surface elevation histories at four points in the chambers at the C3 condition. The wave elevation histories at A, B and C are in phase, but the amplitude at point D is larger than A, B and C with the reflection effect of Shell-1 and anti-phase with the other three points.

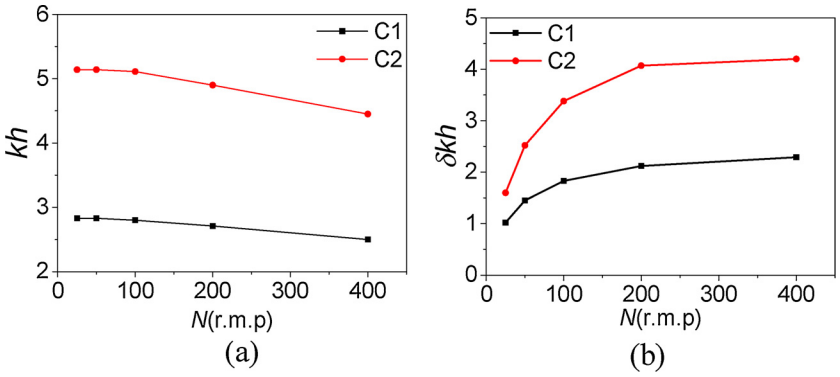

Fig. 15. Distribution of (a) the peak frequency kh and (b) the frequency bandwidth δkh with different turbine speed N.

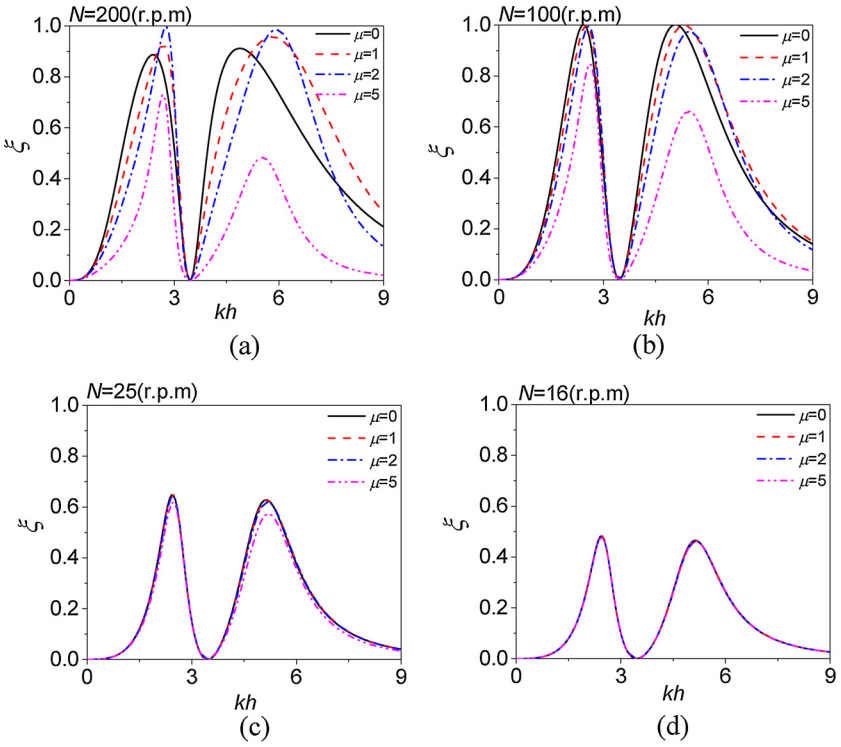

Fig. 16. Effect of chamber volume and turbine blade speed on the efficiency ξ with different kh (a) $N = 200$ (r. m. p) (b) $N = 100$ (r. m. p) (c) $N = 25$ (r. m. p) (d) $N = 16$ (r. m. p).

The distributions of the air pressure and the volume flux in the chamber are given in Fig. 10. It is clear that the amplitudes of the air pressure and the volume flux at C3 are both minimal. This leads to the uncompressed air and minimal net change of air volume in chambers. According to Eq. (6), a lower air pressure in the dual-chamber OWC-WEC corresponds to a lower wave energy transfer capability. This explains why the energy conversion efficiency at C3 in Fig. 7 is minimal.

3.3. Effect of geometrical parameters

In this subsection, effects of the geometrical parameters of the dual-chamber OWC-WEC on the hydrodynamic efficiency are studied, which is important for the structure design. To be specific, the draught of Shell-2 d_2, breadth of the outer chamber $b = R_4 - R_3$, the column radius R_1, and pedestal height T are taken into account.

Firstly, the draught of Shell-2, d_2, is considered. Fig. 11 shows the efficiency distribution of the device, where the value of d_2 varies but the remaining parameters are set as $T/h = 0.1$, $R_1/h = 0.1$, $R_2/h = 0.3$, $d/h = 0.5$, $b/h = 0.15$, $V_0 = \pi d R_5^2$, $d_{wall}/h = 0.01$, $d_1/h = 0.2$, $K = 0.5$, $N = 200$ r.p.m, $h = 10\,m$ and $A/h = 0.1$. Four draughts of Shell-2 are considered, i.e. $d_2/h = 0.1$, $d_2/h = 0.2$, $d_2/h = 0.3$, and $d_2/h = 0.4$. It is found that, as d_2 increases, both the maximal efficiency and the effective frequency bandwidth reduce. Meanwhile, the peak around C2 becomes much slimmer than that around C1. From the above analysis, it is known that the wave motions in the inner and outer chambers contribute to the peaks at C1 and C2, respectively. Thus, the contribution of waves in the outer chamber reduces evidently with the draught of Shell-2. This is clear for curves of $d_2/h = 0.3$ and 0.4, when the draught of Shell-2 is greater than that of Shell-1. The efficiency distribution of the single-chamber OWC-WEC is also given in the figure. It can be seen that the peak efficiency at C1 is smaller than the single-chamber OWC-WEC for the draughts of Shell-2 with $d_2/h = 0.3$ and 0.4. Hence, the draught of Shell-2 should be smaller than Shell-1 in engineering practice.

Further, effects of the outer chamber breadth on efficiency are considered, with geometrical parameters set as $T/h = 0.1$, $R_1/h = 0.1$, $R_2/h = 0.3$, $d/h = 0.5$, $d_1/h = 0.2$, $d_2/h = 0.1$, $d_{wall}/h = 0.01$, $K = 0.5$, $N = 200$ r.p.m, $A/h = 0.1$ and $h = 10$ m. Fig. 12 shows the comparison of four different breadths of the outer chamber, i.e. $b/h = 0.10$, $b/h = 0.15$, $b/h = 0.20$, and $b/h = 0.25$. The breadth of the inner chamber is $b_2/h = 0.20$. It can be seen that the peak frequency of C2 decreases with the breadth of the outer chamber increasing. However, changes in the peak frequency and the frequency bandwidth near C1 are fairly minor compared with that near C2. For a wider outer chamber breadth, longer waves reflected by Shell-1 can be captured by Shell-2 for wave energy conversion. Then, compared with the single-chamber OWC, the frequency bandwidth of 'blind point' region decreases with the increase of the outer chamber breadth. Hence, this suggests that a reasonably wider chamber breadth leads to a greater capability for capturing wave energy.

Fig. 13 shows the efficiency distribution of the device with different shell thickness. Four thickness $d_{wall}/h = 0.01$, 0.02, 0.04 and 0.06 are tested, while the remaining parameters are $T/h = 0.1$, $R_1/h = 0.1$, $R_2/h = 0.3$, $d/h = 0.5$, $d_1/h = 0.2$, $d_2/h = 0.1$, $b/h = 0.15$, $K = 0.5$, $N = 200$ r.p.m, $A/h = 0.1$ and $h = 10$ m. Compared with the above-mentioned two parameters, effects of the shell thickness on the maximal efficiency, effective frequency bandwidth and the peak frequency of the inner air chambers are not sensitive in low frequency domain. However, the effective frequency bandwidth decreases slightly as the increase of the shell chamber in the outer air chamber. Hence, a thinner shell thickness is better for wave energy conversion. From a practical consideration, the shell thickness can be designed by balancing the efficiency and extreme environmental loads.

3.4. Effects of turbine rotate speed and chamber volume

Effects of turbine rotate speed and air compressibility are important factors that determine the gross conversion efficiency from wave motions to electricity. Fig. 14 shows the efficiency distribution of the dual-chamber OWC-WEC, with different turbine rotate speed $N = 25$ (r. m. p), $N = 50$ (r. m. p), $N = 100$ (r. m. p), $N = 200$ (r. m. p) and $N = 400$

(r. m. p). The remaining geometrical parameters are kept as $R_1/h = 0.1$, $R_2/h = 0.3$, $d/h = 0.3$, $d_1/h = 0.2$, $d_2/h = 0.1$, $b/h = 0.15$, $d_{wall}/h = 0.01$, $A/h = 0.1$ and $h = 10$ m. It should be noted that the air parameter is set as $\beta = 0$ for convenience, which stands for a neglection of the air compressibility. It is found that the peak efficiency of C1 and C2 varies with the turbine rotating speed. Form Fig. 14, there is a most fitting speed N which can make a hundred percent energy conversion for both C1 and C2. However, considering the effect of the liquid viscosity in practical engineering, the energy conversion cannot be one hundred percent. Then, Fig. 15 plots the variation of the peak frequency kh and the frequency bandwidth δkh (i.e., the part for $\xi = 0.3$) near both C1 and C2 conditions with different turbine speed N. In Fig. 15(a), as the increase of the turbine rotating speed, the peak frequencies at both C1 and C2 decrease slightly. This characteristic is caused by the long wave carrying more energy which can be used to push higher turbine speed. Form Fig. 15(b), it is clear that the frequency bandwidth of C2 is larger than C1. It also shows that the frequency bandwidth increases largely as the turbine rotating speed near C1 and C2 conditions. Based on the present potential-flow model, it is possible to get the optimal efficiency of power extraction and frequency bandwidth with one specific turbine parameter for one existing dual-chamber OWC-WEC.

For a specific floating OWC-WEC with fixed geometrical parameters, the rotational speed of turbine blades is the main parameter which affects the conversion efficiency. Then, effects of air chamber volume and turbine blade speed are studied with the same geometrical parameters as the above in this section. A dimensionless air chamber volume $\mu = V_0/V$ with $V_0 = \pi d R_5^2$ is set. The condition of $\mu = 0$ lead to $\beta = 0$ which stands for neglecting the effect of the air compressibility. In Fig. 16, the effects of the air chamber volume n on the conversion efficiency is considered under four different rotational speeds of turbine blades, i.e. $N = 200$ (r. m. p), $N = 100$ (r. m. p), $N = 25$ (r. m. p) and $N = 16$ (r. m. p). It should be noticed that the parameter μ should be considered with a small value in practical engineering. For the preliminary theoretical research, the parameter μ can be selected in larger number. From the four figures, it can be seen that chamber volume apparently influences the energy conversion at the condition with higher turbine blade speed. In Fig. 16(d), the effects of the chamber volume can be neglected for lower turbine rotational speed. As the geometrical parameters of the OWC device and turbine are chosen, to some extent, the turbine rotation speed can be regarded as the turbine damping. Under lower turbine damping conditions, the air flow is not compressed evidently, no matter how big the air chamber is. Then it is reasonable to ignore the air compressibility for the lower turbine damping [37]. In Fig. 16(a), the peak frequency is affected slightly by a different value of μ. The frequency bandwidth gets smaller as the increase of the chamber volume for both chambers. And from the variation trend of the efficiency, it can be concluded that there is one optimal chamber volume V_0, which can make the best efficiency of energy power extraction.

4. Conclusions

In this study, a dual-chamber floating concentric cylindrical OWC wave energy converter is proposed for offshore sites. Two chambers are connected at the top of the device, with a self-adapting turbine to generate electricity. A floating pedestal is designed at the bottom of the cylindrical structure to provide buoyancy for the device. Based on the linear potential-flow theory, analytical solutions are derived to investigate hydrodynamic properties of the proposed wave energy converter. The main conclusions can be drawn as follows:

(1) Three typical free-surface oscillation modes in the chambers are found and analyzed. The inner and outer chambers mainly contribute to the efficiency of wave energy conversion for different frequency domains. A bimodal curve which can broaden the frequency breadth effectively is discovered.
(2) The effects of the geometrical parameters of the dual-chamber OWC-WEC on the hydrodynamic efficiency are studied. It is founded that a reasonably wider chamber breadth can leads to a greater capability for capturing wave energy. As an advice for engineering practice, the draught of the outer chamber must be smaller than the inner.
(3) The chamber volume and the parameter of the turbine are studied. It is found that both the volume of the chamber and the rotating speed of turbine can be chosen for the optimal energy conversion. Effects of the chamber volume can be ignored for low damping turbines.

Acknowledgements

This study is supported by the National Natural Science Foundation of China (Grant Nos. 51761135011 and 51709038), the UK-China Industry Academia Partnership Programme (Grant No. UK-CIAPP\73), and the Project funded by China Postdoctoral Science Foundation (No. 2018M630289).

References

[1] S. Astariz, G. Iglesias, The economics of wave energy: a review, Renew. Sustain. Energy Rev. 45 (2015) 397–408.
[2] A.G. Borthwick, Marine renewable energy seascape, Engineering 2 (2016) 69–78.
[3] M.A. Musa, A.Y. Maliki, M.F. Ahmad, W.N. Sani, O. Yaakob, K.B. Samo, Numerical simulation of wave flow over the overtopping breakwater for energy conversion (OBREC) device, Proc. Eng. 194 (2017) 166–173.
[4] J.C. Martins, M.M. Goulart, M. das, N. Gomes, J.A. Souza, L.A.O. Rocha, L.A. Isoldi, E.D. dos Santos, Geometric evaluation of the main operational principle of an overtopping wave energy converter by means of constructal design, Renew. Energy 118 (2018) 727–741.
[5] R. Henderson, Design, simulation, and testing of a novel hydraulic power take-off system for the Pelamis wave energy converter, Renew. Energy 31 (2006) 271–283.
[6] T.V. Heath, A review of oscillating water columns, Philos. Trans. R. Soc. London, Ser. A 370 (2012) 235.
[7] A.F.O. Falcão, Wave energy utilization: a review of the technologies, Renew. Sustain. Energy Rev. 14 (2010) 899–918.
[8] M. Suzuki, C. Arakawa, S. Takahashi, Performance of wave power generating system installed in breakwater at Sakata port in Japan, May 23–28, Toulon, France, Proceedings of the Fourteenth International Offshore and Polar Engineering Conference (2004).
[9] A.F.O. Falcão, The shoreline OWC wave power plant at the Azores, Energicenter Danmark Teknologisk Institut Taastrup (2000) 42–48.
[10] T. Healt, T. Whittaker, C. Boake, The design, construction and operation of the LIMPET wave energy converter (Islay, Scotland), Aalborg, Denmark, 4th European Wave Energy Conference (2000).
[11] A.F.O. Falcão, J.C.C. Henriques, Oscillating-water-column wave energy converters and air turbines: a review, Renew. Energy 85 (2016) 1391–1424.
[12] D.V. Evans, R. Porter, Hydrodynamic characteristics of an oscillating water column device, Appl. Ocean Res. 17 (1995) 155–164.
[13] W. Koo, M.H. Kim, Nonlinear time-domain simulation of a land-based oscillating Water column, J. Water Port Coast. 136 (2010) 276–285.
[14] U. Şentürk, A. Özdamar, Wave energy extraction by an oscillating water column with a gap on the fully submerged front wall, Appl. Ocean Res. 37 (2012) 174–182.
[15] Y. Luo, J.R. Nader, P. Cooper, S.P. Zhu, Nonlinear 2D analysis of the efficiency of fixed Oscillating Water Column wave energy converters, Renew. Energy 64 (2014) 255–265.
[16] D.Z. Ning, J. Shi, Q.P. Zou, B. Teng, Investigation of hydrodynamic performance of an OWC (oscillating water column) wave energy device using a fully nonlinear HOBEM (higher-order boundary element method), Energy 83 (2015) 177–188.
[17] D.Z. Ning, R.Q. Wang, Q.P. Zou, An experimental investigation of hydrodynamics of a fixed OWC Wave Energy Converter, Appl. Energy 168 (2016) 636–648.
[18] I. Simonetti, L. Cappietti, H. Elsafti, H. Oumeraci, Optimization of the geometry and the turbine induced damping for fixed detached and asymmetric OWC devices: a numerical study, Energy (2017) 139.
[19] A. Mora, E. Bautista, F. Méndez, Influence of a tapered and slender wave collector on the increment of the efficiency of an oscillating water column wave-energy converter, Ocean Eng. 129 (2017) 20–36.
[20] S.P. Zhu, L. Mitchell, Diffraction of ocean waves around a hollow cylindrical shell structure, Wave Motion 46 (2009) 78–88.
[21] R.P.F. Gomes, J.C.C. Henriques, L.M.C. Gato, A.F.O. Falcão, Hydrodynamic optimization of an axisymmetric floating oscillating water column for wave energy conversion, Renew. Energy 44 (2012) 328–339.
[22] D.N. Konispoliatis, T.P. Mazarakos, S.A. Mavrakos, Hydrodynamic analysis of three–unit arrays of floating annular oscillating–water–column wave energy converters, Appl. Ocean Res. 61 (2016) 42–64.
[23] R.P.F. Gomes, J.C.C. Henriques, L.M.C. Gato, A.F.O. Falcão, Wave power extraction

of a heaving floating oscillating water column in a wave channel, Renew. Energy 99 (2016) 1262–1275.
[24] A. Elhanafi, G. Macfarlane, A. Fleming, L. Zhi, Experimental and numerical investigations on the intact and damage survivability of a floating–moored oscillating water column device, Appl. Ocean Res. 68 (2017) 276–292.
[25] A.J.C. Crespo, C. Altomare, J.M. Domínguez, J. González-Cao, M. Gómez-Gesteira, Towards simulating floating offshore oscillating water column converters with Smoothed Particle Hydrodynamics, Coast. Eng. 126 (2017) 11–26.
[26] A. Elhanafi, A. Fleming, G. Macfarlane, L. Zhi, Underwater geometrical impact on the hydrodynamic performance of an offshore oscillating water column–wave energy converter, Renew. Energy 105 (2017) 209–231.
[27] Y. Washio, H. Osawa, Nagata Y, H. Furuyama, T. Fujita, Offshore floating type wave power device "mighty whale" open Sea tests, Oceans 4 (2002) 1860–1866.
[28] K. Rezanejad, J. Bhattacharjee, C.G. Soares, Stepped sea bottom effects on the efficiency of nearshore oscillating water column device, Ocean Eng. 70 (2013) 25–38.
[29] K. Rezanejad, J. Bhattacharjee, C.G. Soares, Analytical and numerical study of dual-chamber oscillating water columns on stepped bottom, Renew. Energy 75 (2015) 272–282.
[30] F. He, J. Leng, X. Zhao, An experimental investigation into the wave power extraction of a floating box-type breakwater with dual pneumatic chambers, Appl. Ocean Res. 67 (2017) 21–30.
[31] R. Wang, D. Ning, C. Zhang, Numerical investigation of the hydrodynamic performance of the dual-chamber oscillating water columns, June 25–30, San Francisco, USA, Proceedings of the Twenty-Seventh International Ocean and Polar Engineering Conference (2017).
[32] D. Ning, R. Wang, C. Zhang, Numerical simulation of a dual-chamber oscillating Water column wave energy converter, Sustainability 9 (2017) 1599.
[33] A.F.O. Falcão, J.C.C. Henriques, Model-prototype similarity of oscillating-water-column wave energy converters, Int. J. Mar. Energy 6 (2014) 18–34.
[34] W. Sheng, R. Alcorn, A. Lewis, On thermodynamics in the primary power conversion of oscillating water column wave energy converters, J. Renew. Sustain. Energy 5 (2013) 1257–1294.
[35] P.R.F. Teixeira, D.P. Davyt, E. Didier, R. Ramalhais, Numerical simulation of an oscillating water column device using a code based on Navier–Stokes equations, Energy 61 (2013) 513–530.
[36] H. Martins-Rivas, C.C. Mei, Wave power extraction from an oscillating water column at the tip of a breakwater, J. Fluid Mech. 626 (2009) 395–414.
[37] A. Elhanafi, G. Macfarlane, A. Fleming, L. Zhi, Scaling and air compressibility effects on a three-dimensional offshore stationary OWC wave energy converter, Appl. Energy 189 (2017) 1–20.
[38] Y. Zhou, C. Zhang, D. Ning, Hydrodynamic investigation of a concentric cylindrical OWC wave energy converter, Energies 11 (2018) 985.
[39] H. Martins-Rivas, C.C. Mei, Wave power extraction from an oscillating water column along a straight coast, Ocean Eng. 36 (2009) 426–433.
[40] A.J.N.A. Sarmento, A.F.O. Falcão, Wave generation by an oscillating surface-pressure and its application in wave-energy extraction, J. Fluid Mech. 150 (1985) 467–485.
[41] D.N. Konispoliatis, S.A. Mavrakos, Hydrodynamic analysis of an array of interacting free-floating oscillating water column (OWC's) devices, Ocean Eng. 111 (2016) 179–197.
[42] S.P. Zhu, L. Mitchell, Combined diffraction and radiation of ocean waves around an OWC device, J. Appl. Math. Comput. 36 (2011) 401–416.
[43] D.V. Evans, R. Porter, Efficient calculation of hydrodynamic properties of OWC-type devices, J. Offshore Mech. Arct. 119 (1997) 210–218.
[44] B. Teng, R.E. Taylor, New higher-order boundary element methods for wave diffraction/radiation, Appl. Ocean Res. 17 (1995) 71–77.